IEEE Access
Multidisciplinary ⁝ Rapid Review ⁝ Open Access Journal

Received April 30, 2020, accepted May 18, 2020, date of publication June 4, 2020, date of current version June 17, 2020.

Digital Object Identifier 10.1109/ACCESS.2020.2999894

Mapping the Physical and Dielectric Properties of Layered Soil Using Short-Time Matrix Pencil Method-Based Ground-Penetrating Radar

NATTAWAT CHANTASEN[1], (Member, IEEE), AKKARAT BOONPOONGA[1], (Member, IEEE), KRIT ATHIKULWONGSE[2], (Member, IEEE), KAMOL KAEMARUNGSI[2], (Senior Member, IEEE), AND PRAYOOT AKKARAEKTHALIN[1], (Member, IEEE)

[1]Research Center of Innovation Digital and Electromagnetic Technology, Department of Electrical and Computer Engineering, Faculty of Engineering, King Mongkut's University of Technology North Bangkok, Bangkok 10800, Thailand
[2]National Electronics and Computer Technology Center, National Science and Technology Development Agency, Pathumthani 12120, Thailand

Corresponding author: Akkarat Boonpoonga (akkarat.b@eng.kmutnb.ac.th)

This work was supported in part by the Thailand Research Fund through the TRF Senior Research Scholar Program under Grant RTA6080008, and in part by the National Science and Technology Development Agency through the Thailand Graduate Institute of Science and Technology (TGIST) under Grant SCA-C0-2558-1031-TH.

ABSTRACT This paper presents the mapping of the physical and dielectric properties of layered soil by using ground-penetrating radar (GPR). Poles extracted from the GPR signals by using the short-time matrix pencil method, along with preprocessing, including filtering and antenna calibration, were employed in order to map the physical and dielectric properties of the layered soil. With the proposed system, the conjugate gradient method was also introduced to solve the time-domain inverse problem faced in the antenna calibration. Experimentations were conducted on four different days in Nakhon Ratchasima province in Thailand, which is a potential area for the occurrence of hardpan. These were done based on the hypothesis that the soil properties, such as water content and dielectric constant, should change when the experimentation day changes in spite of the experimentations in the same area. In the experimentations, soil samples were collected using a core method, and their physical and dielectric properties were measured by using a standard laboratory method and a commercial dielectric probe kit. The measured soil properties and extracted poles for each experiment and each soil layer are shown and analyzed. The results indicate that the real part of the dielectric constants, strongly related to water content, can be mapped using extracted natural frequency. In order to map the dielectric properties, i.e. the water content and dielectric constants of the layered soil, the experimental results were fitted to 2nd-order polynomial curve. The largest regression value of the fitted curve was 0.9994. The bulk density, which is a physical property of the soil, distinguishes the soil type here differentiated by different soil layers. According to the experimental results, the hardpan occurred at the second soil layer because its bulk density was higher than 1.8 g/cm^3. The bulk density was mapped by extracted poles, including damping factors and natural frequencies.

INDEX TERMS Dielectric property, permittivity estimation, layered soil, ground-penetrating radar, GPR, short-time matrix pencil method.

I. INTRODUCTION

Tapioca has been considered one of the most important economic crops of Thailand. According to a report of the Thai Tapioca Starch Association, the annual production of tapioca in Thailand is about 30 million tons. Tapioca is generally planted in the same area for a long time annually using heavy machinery without proper soil improvement. This potentially results in soil compaction, which becomes a problem for the tapioca growth [1]. Soil compaction or subsoil compaction, sometimes called hardpan, mainly impedes the drainage of water and restricts the growth of plant roots and also causes tuber rot. In order to resolve the underlying problems, one can use a deep tillage tool, such as a subsoiler or ripper, in order to break up the soil compaction so that the plant roots can grow. Because of the high cost of tillage tools, it is important

The associate editor coordinating the review of this manuscript and approving it for publication was Francesco Benedetto.

to ensure that the hardpan really exists and to know the actual depth and extent of the hardpan layer.

A simple way to observe the hardpan occurrence is to use a spade to dig up a section of the soil along with the tapioca roots. An accurate method to investigate hardpan is core method, in which soil core samples are collected for analyzing in a laboratory. However, these two methods not only destroy the soil surface but also are labor-intensive processes. Another alternative less invasive way to detect a compacted layer is by using a soil penetrometer. The main disadvantages of the penetrometer are the difficulty of separating the point and skin friction resistances and it takes a long time to operate it. It is also not suitable for operation in wide areas of agriculture. Bulk density, which is a standard tool used to identify the hardpan layer, is in the range of 1.8 to 2.0 g/cm^3 or even higher [2]. Typically, bulk density of soil can be obtained by using a laboratory measurement. However, it is restricted to small observation areas and is very time consuming. Moreover, the sampling point of the soil cannot be a representative of the entire agriculture area. Thus, there is a need for non-invasive and efficient tool that can identify hardpan and is suitable for precision agriculture in wide areas. Besides hardpan identification, knowledge of the soil water content strongly related to the dielectric property of the soil is also essential for agriculture application as well.

Over the past two decades, there have been several attempts to estimate the water content of soil surfaces by using airborne and spaceborne remote-sensing methods with either passive microwave radiometry or active radar instruments [3]. These methods are efficient for large areas. The Soil Moisture and Ocean Salinity (SMOS) mission, which originated from the European Space Agency (ESA), has provided the measurement of brightness temperatures with a three-day global revisit time [4]–[6]. Subsequently, the Soil Moisture Active Passive (SMAP) mission was launched by the National Aeronautics and Space Administration in order to estimate the soil moisture with a 9-km resolution and a three-day revisit time [7], [8]. Although the SMOS and SMAP missions have been successful, they can measure the soil moisture of the ground surface or a layer of a few centimeters and achieve only low-resolution measurements. Estimating the water content of layered soil at a deeper depth with a high-resolution measurement for precision agriculture is still a very challenging task.

One of the most promising technologies employed for characterizing the electrical property of soil is ground-penetrating radar (GPR). GPR is a geophysical non-destructive method that transmits short pulses and then receives the reflected responses in order to image the subsurface. With the increase in demand for several applications related to underground survey, GPR has become an intelligent sensor system [9]–[11]. A number of researches have been done to investigate the potential of GPR for estimating soil moisture. The classification and prediction of the water content of subsurface have been developed on the basis of the use of GPR along with the deep neural network technique [12]. A-scan time-series data were taken as the input data to achieve the outputs, including moisture quantitative classification and volume water content. Based on GPR, a common midpoint method was proposed to measure the dielectric permittivity that is strongly dependent upon the soil water content, by deriving the velocity of waves that are propagated through the dielectric medium [3], [13]. This method performs several measurements for a single profile characterization by varying the distance between the transmitting and receiving antennas and is therefore not applicable to a real-time operation. Recently, we proposed a method that can estimate the permittivity of a layered medium by utilizing the reflections from individual layers. In this approach, it was assumed that the permittivity of the layered medium was real. The attenuation of the traveling wave was therefore not taken into account [14]. However, the attenuation of a wave traveling through layered soil naturally exists.

Other approaches using the frequency spectra of the received GPR signals were proposed in order to characterize the target [15]–[17]. Several attempts for railway-ballast monitoring and assessment have been based on the frequency-based evaluation of porous media [16], [18]–[21]. In [16], the magnitude spectrum was used as a feature and then classified by using a support vector machine (SVM) for railway-ballast assessment. The effects of the different physical conditions of ballast on the electromagnetic response of the material were analyzed for each scenario using time- and frequency-domain signal processing techniques [18]. In 2017, the assessment of geometric features of the ballast aggregates within a railway track-bed was proposed [20]. In this approach, spectral analyses of the 2GHz GPR data were performed in the frequency domain. The spectral response of the GPR data in the frequency domain was analyzed in the case of mono-sized single- and multi-particle configurations of round-shaped ballast aggregates with different diameters and electric properties. A signal processing method performed in the frequency domain was proposed to estimate the moisture content in a porous medium [17]. In this approach, the results showed that the signal spectra obtained from the GPR measurement of the medium with different moisture content were different.

However, the quality factor (Q-factor) of soil is generally low; thus, it is not appropriate for estimating soil moisture content and discriminating the soil type directly through the frequency response. An example of the potential frequency response of soil is shown in Fig. 1 in which its peak is not notable. We also proposed the use of poles extracted from the GPR frequency response by using the short-time matrix pencil method (STMPM) in order to automatically detect and classify buried improvised explosive devices (IEDs) [22].

This paper proposes the use of poles to map the physical and dielectric properties of the layered soil, instead of directly using the frequency response whose Q-factor is generally low. Poles including natural frequencies and damping factors were extracted by using the STMPM. In Section II, a ground-penetrating radar-based identification using the STMPM

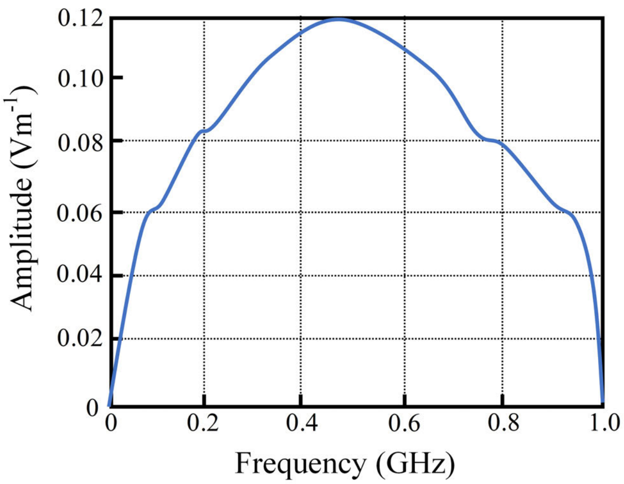

FIGURE 1. Example of the potential frequency response of soil.

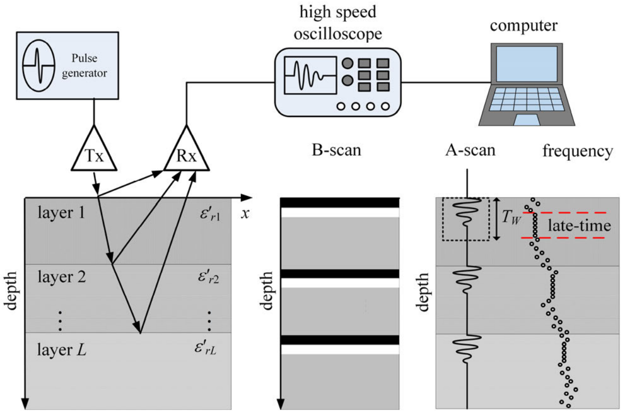

FIGURE 2. Ground-penetrating radar-based identification system.

was presented, along with the conjugate gradient method used to solve the inverse problem, and preprocessing with antenna calibration was used to reduce the antenna effects. In Section III, the experiments for collecting soil samples and GPR signals are described. The results and discussion of the standard laboratory and proposed GPR system are shown in Section IV. The soil properties, including water content, dielectric constant, and bulk density, were mapped to poles extracted by using the STMPM. We employ preprocessing, i.e., filtering and antenna calibration, before performing the STMPM. In order to map the soil properties, 2$^{\text{nd}}$-order polynomial was generated. Finally, conclusions are drawn in Section V.

II. GROUND-PENETRATING RADAR-BASED IDENTIFICATION

GPR is a geophysical electromagnetic instrument that can image a subsurface. In this paper, we propose the use of GPR to characterize the physical and dielectric properties of the layered soil. Figure 2 depicts a ground-penetrating radar-based identification system. A short monocycle pulse was generated and transmitted via a transmitting antenna.

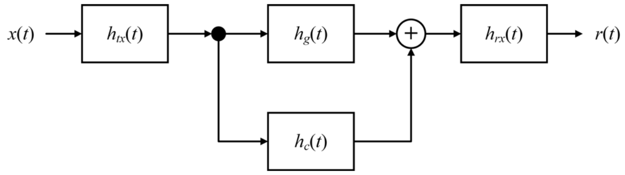

FIGURE 3. Diagram of impulse responses of GPR system.

The transmitted pulse is propagated through the antenna and penetrates into the ground. The pulse signal reflected from the interface of each medium layer is then received by a receiving antenna. The received pulse was digitized and captured by using a high-speed oscilloscope. The sampling rate has to be at least twice the maximum frequency, corresponding to the Nyquist theorem. The captured data were fed to a computer in order to perform signal processing. Antenna calibration was performed in order to reduce the antenna effect resulting in the pulse dispersion [23]. A STMPM was then exploited to extract poles, which are tools for identifying the property of the soil.

A. ANTENNA CALIBRATION

Antenna calibration is first needed to resolve the pulse dispersion due to the variation in the antenna response. The influence factor associated with antenna effect also degrades the vertical resolution in imaging the shallow subsurface. Since the GPR proposed in this paper operates in a time domain by transmitting and receiving a short pulse, the antenna calibration had to be done in a time domain as well. Let us reconsider Fig. 2 as a system block diagram shown in Fig. 3. The impulse response of the total system can be expressed as

$$h_T(t) = h_{tx}(t) * h_g(t) * h_{rx}(t) + h_{tx}(t) * h_c(t) * h_{rx}(t) \tag{1}$$

where $h_{tx}(t)$, $h_{rx}(t)$, and $h_g(t)$ represent the impulse responses of the transmitting and receiving antennas, and the object, respectively. Here, the object under consideration is the layered soil. The effect of free space loss was not taken into account because poles are aspect-independent parameters [24]. The $h_c(t)$ denotes the impulse response of the mutual coupling between the transmitting and receiving antennas. Operation $*$ denotes the convolution. The right-hand side term of (1) is the response, including the mutual coupling and the individual antenna characteristic. In practice, this term can be obtained by measuring in an empty room without any object as given by

$$h_{empty}(t) = h_{tx}(t) * h_c(t) * h_{rx}(t). \tag{2}$$

Substitute (2) into (1) and then arrive at

$$h_T(t) - h_{empty}(t) = h_{tx}(t) * h_g(t) * h_{rx}(t). \tag{3}$$

Note that the impulse responses of the transmitting and receiving antennas still appear in (3). In order to eliminate these responses, i.e. $h_{tx}(t)$ and $h_{rx}(t)$, there is a need for one more relevant equation. A measurement of a large metal sheet placed on a ground surface was carried out for reference. The reference metal sheet is assumed to perfectly reflect all incident electromagnetic waves. Thus, we can set the impulse response of the reference metal sheet to be -1, namely $h_g(t) = -1$. The impulse response of the total system when placing the metal sheet on the ground surface is denoted by $h_T(t) = h_{ref}(t)$ and then given as

$$h_{ref}(t) - h_{empty}(t) = h_{tx}(t) * (-1) * h_{rx}(t). \tag{4}$$

The transmitting and receiving antenna characteristics, i.e. $h_{tx}(t)$ and $h_{rx}(t)$, must be deconvolved from the total impulse response $h_T(t)$. According to (3) and (4), the impulse response of the object can be expressed as

$$h_g(t) = (h_{ref}(t) - h_{empty}(t))^{-1} * (h_T(t) - h_{empty}(t)). \tag{5}$$

After sampling, the time variable t was replaced by nT_s where T_s and n denote the sampling period and time index, respectively. The impulse response of the object is expressed as

$$h_g(nT_s) = (h_{ref}(nT_s) - h_{empty}(nT_s))^{-1} * (h_T(nT_s) - h_{empty}(nT_s)). \tag{6}$$

To solve this equation, the direct inversion of the convolution operation results in numerical instabilities due to the presence of noise in the data [25], [26]. Thus, this paper introduces the use of the conjugate gradient method in order to solve the deconvolution. This equation can be rewritten in a compact matrix form of the inverse problem as

$$[x] = [A]^{-1}[y] \tag{7}$$

where $x = h_g(nT_s)$, $A = h_{ref}(nT_s) - h_{empty}(nT_s)$, and $y = h_T(nT_s) - h_{empty}(nT_s)$. The matrix [A] is arranged as a rotated Toeplitz matrix formed from the subtraction between the impulse responses of the reference and empty room measurements as follows:

$$[A] = \begin{bmatrix} a[NT_s] & a[NT_s - T_s] & \cdots & a[3T_s] & a[2T_s] & a[T_s] \\ a[NT_s - T_s] & a[NT_s - 2T_s] & \cdots & a[2T_s] & a[T_s] & 0 \\ a[NT_s - 2T_s] & a[NT_s - 3T_s] & \cdots & a[T_s] & 0 & 0 \\ \vdots & \vdots & \vdots & \vdots & \vdots & \vdots \\ a[2T_s] & a[T_s] & \cdots & 0 & 0 & 0 \\ a[T_s] & 0 & \cdots & 0 & 0 & 0 \end{bmatrix} \tag{8}$$

where N is the total number of samples of an A-scan signal and $a[NT_s] = h_{ref}(NT_s) - h_{empty}(NT_s)$. In order to find the matrix $[x]$, the functional $F(x) =< Ax - y, Ax - y >$ is minimized based on the conjugate gradient by searching along a set of direction vectors p_k instead of solving the inverse problem directly.

An initial guess was selected as $x = x_0$ and then the error residual $r_0 = y - Ax_0$ was therefore accordingly generated. The initial search direction vector was $p_0 = A^H r_0$, where operation ^{H} denotes the complex conjugate transpose. The update equation can be written as follows:

$$c = \frac{\|A^H r_k\|^2}{\|Ap_k\|^2} \tag{9}$$

$$x_{k+1} = x_k + cp_k \tag{10}$$

$$r_{k+1} = y - Ax_k = r_k - cAp_k \tag{11}$$

$$b = \frac{\|A^H r_{k+1}\|^2}{\|A^H r_k\|^2} \tag{12}$$

$$p_{k+1} = A^H r_{k+1} - bp_k \tag{13}$$

The iterative loop will be halted when the error residue is below the predetermined value of $||r_k||$. However, there is no case that requires more iteration than the dimension of $[A]$ in the absence of round-off errors

B. POLE EXTRACTION USING THE SHORT-TIME MATRIX PENCIL METHOD

The basic idea of the STMPM is to move a time window through the entire signal. The minimum time step is the time interval between successive samples. Matrix pencil-method is employed to extract poles and residues from each time window. The extracted poles and residues are indexed by the starting point of the time window. A time axis is added to the complex plane to create a time-frequency space. The late-time part begins from the point at which the extracted poles converged to stable constant values. Real and imaginary parts of poles and residues of CNRs are separately plotted versus the sliding time.

The total received signal obtained after performing the antenna calibration can be given as

$$r'(t) = x(t)h_g(t). \tag{14}$$

Based on the singularity expansion method (SEM), the time-domain signal reflected from an object excited by a short pulse can be divided into two successive portions as expressed by

$$r'(t) = r'_{ET}(t_s) + r'_{LT}(t) + \eta(t) \tag{15}$$

where $r'_{ET}(t)$, $r'_{LT}(t)$, and $\eta(t)$ are the early-time and late-time portions of the received signal, and the noise in the system, respectively. The first signal portion is the direct reflection due to the wave impingement on the object's surface. The second one was employed to extract the pole results from the resonance phenomena of the object. With the SEM principle, the formulation for modeling the late-time portion is

$$r'_{LT}(t) = \sum_{i=1}^{M} R'_i e^{s_i t} + \eta(t) \tag{16}$$

where $s_i = \alpha_i \pm j\omega_i$ denotes an i^{th} pole, including damping factor α_i and natural angular frequency ω_i. The R'_i and M denote residue, which is a complex amplitude and the number of poles, respectively. According to [27], in order to extract poles using the STMPM, a window with the length of T_w was moved along the time variable. The windowed signal of the late-time portion can be given by

$$r'_{T_{TL}}(t) \approx \text{Re}\left(\sum_{m=1}^{M} R_m^{'T_{TL}} e^{s_m(t - T_{TL})}\right) \tag{17}$$

FIGURE 4. **Collecting soil samples.**

where T_{LT} denotes the shifting time and

$$R_m^{'T_{TL}} = R'_m e^{s_m T_{TL}} = R'_{m e^{(-\alpha_m + j\omega_m)T_{TL}}}. \tag{18}$$

In a natural logarithmic scale, (18) can be rewritten as

$$Ln(|R_m^{'T_{TL}}|) = Ln(|R'_m|) - \alpha_m T_{TL}. \tag{19}$$

From (19), the logarithmic magnitude of the residues linearly decreases versus T_{LT} with slope α_m. The slope of the logarithm of the residues can be calculated, which is equal to the damping factor needed.

III. EXPERIMENTS

In this section, experiments using the standard laboratory method and the proposed GPR system were conducted in order to determine the relationship between their results. With the standard laboratory method, it is necessary to extract layered soil samples from the ground in order to measure their physical and dielectric properties. In contrast, GPR, which is one of the most popular non-destructive methods, can measure the dielectric properties of the subsurface *in situ* without extracting soil from the ground. Experiments using both methods were conducted on four different days in two different months in Nakhon Ratchasima province, which is a potential area for the occurrence of hardpan in Thailand. The average weekly rainfalls on four days of the experiments were 1.13, 9.71, 0.44, and 0.0 mm and their relative humidity was 79, 89, 86, and 83%, respectively.

A. SOIL SAMPLE COLLECTION

Soil samples were collected at 5-cm increments to a depth of 80 cm by using the core method. Figure 4 shows the collecting of soil samples by pressing the volumetric cylinder into the soil. Collecting the soil was simultaneously repeated two times along two different soil sampling lines in order to increase the accuracy of the soil measurement. The total volume of the soil core sampler was 150.77 cm^3, equivalent to that of the collected soil. In order to measure the water content and bulk density of the soil, the wet soil collected from the field was weighed and dried for 24 hours in an oven operating at 105°C. The dry soil obtained after oven drying was weighted again to attain the weight of the soil without water. The water content of the soil can was calculated by using

$$\theta_s = (W_s - W_d)/(W_d - W_c) \tag{20}$$

where θ_s is the soil water content in % by weight, W_s is the weight of the wet soil sample before oven drying in g, W_d is the weight of the soil sample after oven drying in g, and W_c is the weight of the soil core sampler in g. The bulk density of the soil can be given by

$$\rho_b = ((W_d + W_c) - W_c)/V_c \tag{21}$$

where ρ_b is soil bulk density in g/cm^3, and V_c is the volume of the soil core sampler in cm^3.

The dielectric property of the soil samples was also measured by using the N9923A FieldFox handheld RF vector network analyzer (VNA), along with the dielectric probe and N1500A Materials Measurement Suite software. Figure 5 shows the measurement setup for the dielectric constants. The average of the dielectric constants measured between 800 and 1000 MHz was collected in order to find the relationship of the dielectric and physical properties of the layered soil.

B. GROUND-PENETRATING RADAR EXPERIMENTS

In this section, we explain the use of GPR to collect the signals reflected from underground. The received signals were utilized to characterize the soil's property on the basis of the SEM principle. Figure 6 shows the experimental setup of the GPR. A monocycle pulse whose pulse width was equal to 0.9 ns was generated by using a pulse generator, model AVB1-3, and then transmitted via a transmitting antenna. The signals reflected from underground and directly propagated through the air were received by using a receiving antenna. The antennas employed as transmitting and receiving antennas were Scutcheon antennas [28]. The measured return loss of the antennas was below −10dB in the range of 410 MHz to 12 GHz. The measured gains at the frequency of 460 and 960 MHz were 2.0 and 4.8 dBi, respectively. The antennas were placed at the height h_{ant} of 5 cm above the ground.

The received signals were captured and digitized by using a high-speed oscilloscope, part no. DSOX6004A. The sampling frequency of the oscilloscope was 20 Gsps. The digitized signals were fed to a computer in order to perform signal processing. In order to observe the soil's physical properties, such as soil structure, color, and depth, it was necessary to dig a cubic hole, as shown in Fig. 6. As seen in the figure, there are three different layers distinguished by different colors and

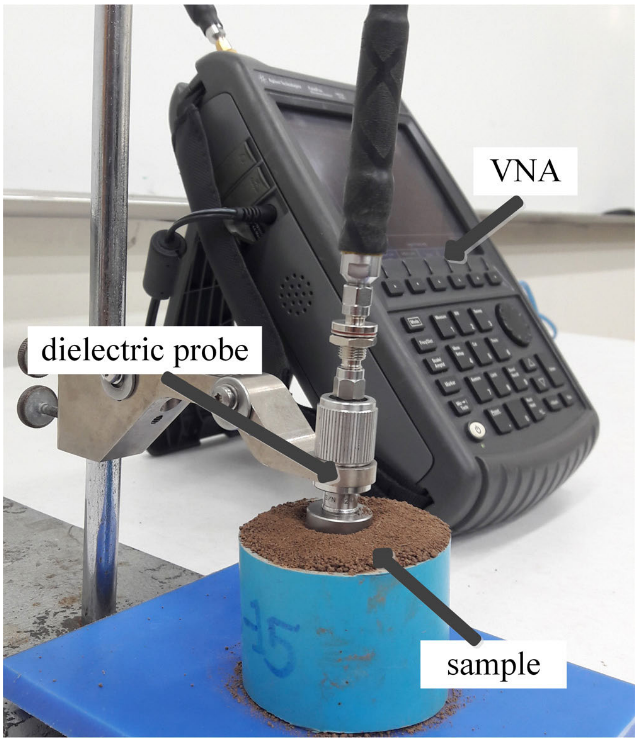

FIGURE 5. Measurement setup using a commercial dielectric probe kit.

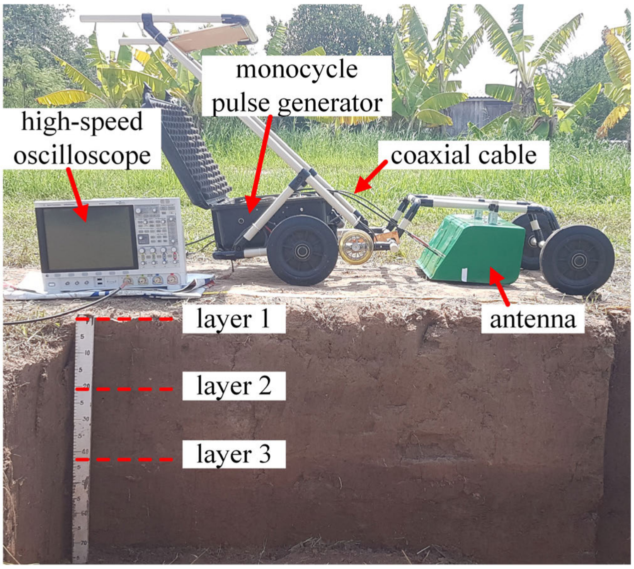

FIGURE 6. Experimental setup of the proposed GPR.

soil types. The interfaces of the individual layer were at the depth of about 20 and 40 cm.

IV. RESULTS AND DISSCUSSION

A. SOIL SAMPLE ANALYSIS

The water content and bulk density of the soil samples were measured by using the standard laboratory method, as described in the previous section. Figure 7 depicts the measured water content of the soil samples collected at 5-cm increments to a depth of 75 cm. In the figure, as the depth increases, the water content increases as well. At each soil depth, there is a significant difference in the water content measured on each day. This is because collecting the soil samples was conducted on different days. The soil water contents resulted from associated factors such as rainfall and were therefore different. Figure 8 depicts the measured bulk density of the soil samples. The figure shows that the bulk density was greater than 1.8 g/cm^3 when the depth was around 20 cm to 40 cm. This reveals that the soil at this depth interval was hardpan. The bulk densities obtained from the measurement on different days were almost identical because the varying amount of rainfall did not impact the bulk density. Moreover, it also implies that soil bulk density does not directly relate to soil water content. It does not change as the small amount of water content changes.

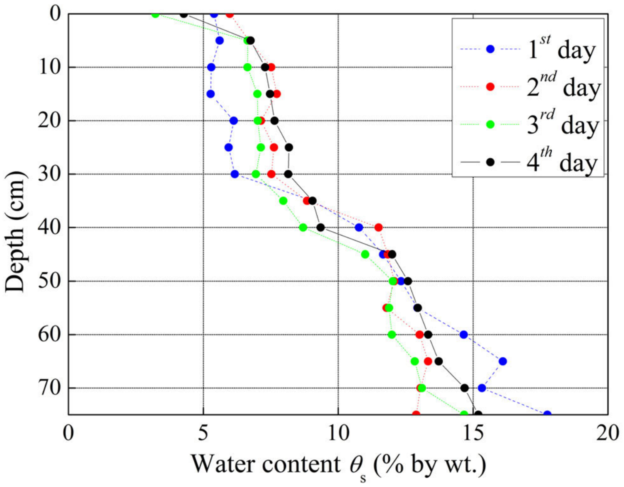

FIGURE 7. Water content of soil samples.

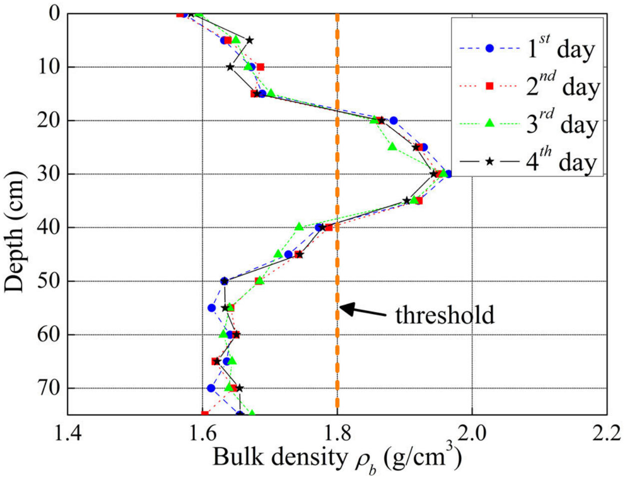

FIGURE 8. Bulk density of soil samples.

Figure 9 depicts the dielectric constants measured from the collected soil samples by using a commercial dielectric probe kit. In Fig. 9 (a), the real parts of the measured dielectric constants increase proportionally with the depth and were

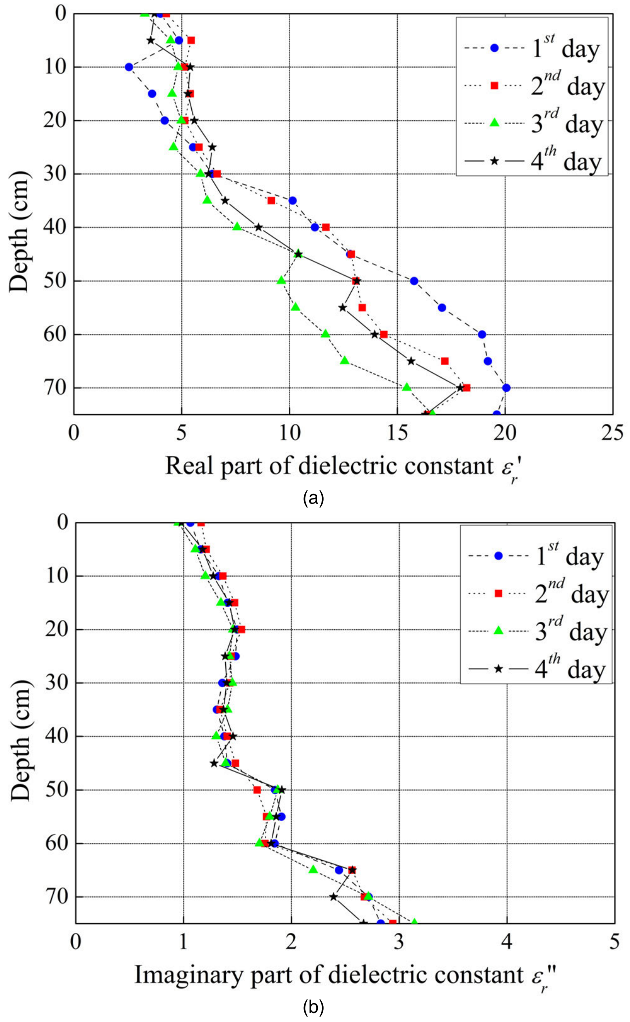

FIGURE 9. Measured dielectric constants of soil (a) real part (b) imaginary part.

different in the four different days of the experiments. Note that this behave like the water content of the layered-soil samples. It was well known that the real part of dielectric constant is strongly related to the water content of the soil [29]. Figure 9 (b) depicts the imaginary parts of the dielectric constants obtained from the measurement of the collected soil samples. These results obtained on four different experimentation days are almost identical and slightly increased when the depth increased. This implies that we cannot use the imaginary parts of the dielectric constants in order to map the physical and dielectric properties of layered soil.

B. GPR RESULTS

The experiments with the proposed GPR system were conducted as described in details in the previous section. The GPR was moved along in the direction of the cubic dug hole with a step interval of $\Delta x = 5$ cm to collect each A-scan signal and then to form the GPR B-scan image. The experiments were performed on the same four days in the same area where the soil samples were collected. Collecting the signals at each interval step was repeated six times and averaged for increasing accuracy and reliability. Figure 10 depicts examples of the GPR B-scan image and the extracted poles obtained from one of the experimentation days. The pre-processing, such as filtering and antenna calibration, was performed before pole extraction was done by using STMPM. In the GPR B-scan images, the dielectric constant of the layered soil was assumed to be $\varepsilon'_r = 6$ in order to transform the time axis to a depth axis. As seen in the figure, the interfaces of the individual soil layers were at around 4, 18, and 42 cm, not exactly coinciding with the real layer interfaces. This is because the depth under consideration was a virtual depth. The dielectric constant used to transform the time axis to a depth axis was assumed to be real and constant. In practical terms, the dielectric constant of the soil will vary and depend upon the depth and soil type. The layer interface appearing at 4 cm resulted from performing the antenna calibration, reducing the effects due to the antenna response and strong mutual coupling between the transmitting and receiving antennas. During the procedure of the antenna calibration, the large metal plate was placed on the top of the soil surface and GPR was used to collect the signal from the reflection of the metal plate. This signal was used as a reference for performing the antenna calibration of (6) along with the conjugate gradient method used to solve the inverse problem in the time domain.

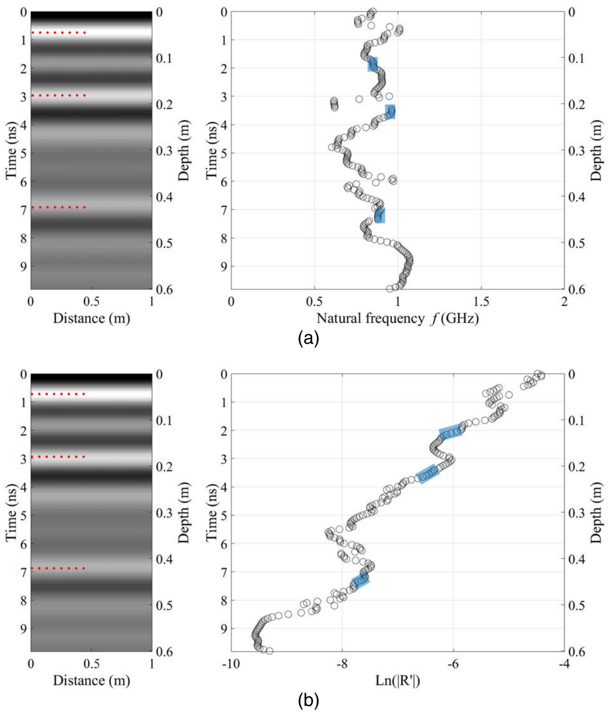

FIGURE 10. GPR B-scan images and (a) extracted natural frequency (b) magnitude of residues.

Figure 10 (a) and (b) also depict examples of the extracted natural frequencies and the magnitude of the residue, respectively. The simple late-time estimation method was applied to find the commencement of the late-time response, following [20]. In the figure, the shaded area denotes the region of the four selected natural frequencies and the magnitude of the

TABLE 1. Extracted poles and measured properties of layered soil.

Soil samples		Damping factor σ_1 (GHz)	Natural frequency f_1 (GHz)	Real part of dielectric constant ε_r'	Imaginary part of dielectric constant ε_r''	Water content θ_s (% by weight)	Bulk density ρ_b (g/cm^3)
layer 1	1st day	-0.4106	0.8521	4.01744	1.06333	5.3985	1.57254
	2nd day	-0.3762	0.8385	4.2888	1.16333	5.98111	1.56684
	3rd day	-0.4404	0.9462	3.28891	0.95171	3.22466	1.59474
	4th day	-0.3905	0.9102	3.73981	0.98011	4.2765	1.58317
layer 2	1st day	-0.6119	0.9622	4.21265	1.49649	6.12732	1.88349
	2nd day	-0.5897	0.8687	5.14821	1.53755	7.13561	1.86312
	3rd day	-0.5624	0.8549	5.58393	1.45797	7.01828	1.85476
	4th day	-0.5797	0.8371	4.9838	1.47327	7.64271	1.87572
layer 3	1st day	-0.5180	0.8836	11.17828	1.37845	10.7706	1.77272
	2nd day	-0.5215	0.8492	11.69186	1.40505	11.49926	1.78761
	3rd day	-0.5050	0.9465	7.57216	1.30279	8.69926	1.74334
	4th day	-0.5090	0.9334	8.56542	1.45803	9.35082	1.77815

TABLE 2. Variances of extracted poles and measured properties of layered soil.

Variances		Damping factor σ_1 (GHz)	Natural frequency f_1 (GHz)	Real part of dielectric constant ε_r'	Imaginary part of dielectric constant ε_r''	Water content θ_s (% by weight)	Bulk density ρ_b (g/cm^3)
among	of						
four days	layer 1	0.000772	0.0025	0.1822	0.0090	1.4945	0.000151
	layer 2	0.000427	0.0031	0.3273	0.0012	0.3973	0.000164
	layer 3	0.000588	0.0020	3.9857	0.0042	1.6431	0.000364
three layers	four days	0.007125	0.002184	10.9761	0.0580	7.8734	0.0219

residue at the late-time response, whose commencement was at $t_{LT} = 1.8$, 3.45 and 7.15 ns for the first, second, and third soil layers. In Fig. 10 (b), the shaded area indicating the range of the constant slope of the line was fitted to the natural logarithm of the magnitudes of the residue by linear regression in order to ascertain the damping factor [27]. The average of the four selected poles, including natural frequencies and the damping factor, was $s_1 = -0.4106 \pm j0.8521$, $-0.6119 \pm j0.9622$, and $-0.5180 \pm j0.8836$ GHz for the first, second, and third soil layers, respectively.

Table 1 lists the extracted poles and measured properties of the layered soil. The individual extracted natural frequency listed in the table was obtained from the average of the four successive natural frequencies at the late time of each soil layer on each experimentation day. The measured soil properties, i.e. the real and imaginary part of the dielectric constant, water content, and bulk density, obtained from the commercial dielectric probe kit and standard laboratory method were listed from the interface position of the layered soil. These results were different according to the experimentation days and soil layers. It is too difficult to discuss in greater details on the value changes. Thus, we calculated the variances from the underlying tables in order to compare the difference of each experimental result as seen in Table 2. Some examples of the discussions for the table are as follows.

According to Table 2, we chose the threshold of a variance at 0.001; therefore, the variance greater than or equal to 0.001 indicates a significant difference in the experimental results under consideration. The results can be used to manipulate the equations of their relationship. In Table 2, the variances of the bulk density among the four experimentation days of the first, second, and third layers were 0.000151, 0.000164, and 0.000364, respectively. The number of zero digits after the decimal point in these variances was three, indicating that the difference in the bulk density of each soil layer on the four different experimentation days was very small. These variances were not large enough, implying that the bulk densities on the four different experimentation days were almost identical, corresponding to the bulk density plotted in Fig. 8. On the other hand, the variance of the bulk density among the three soil layers on the four experimentation days was 0.0219 greater than the threshold. The bulk density of the soil layers was significantly different, corresponding to that of each layer plotted in Fig. 8 as well. Normally, the soil in each layer is of a same type, Thus, it may be possible to use bulk density to differentiate the soil type among layers, but cannot estimate the water content that was changed by the experiment.

Another example being discussed here was the variances in the damping factors extracted by using STMPM. As seen in Table 2, the variances in the damping factors among the four experimentation days involving the first, second, and third layers were 0.000772, 0.000427, and 0.000588, respectively. These values were somewhat small. This implies that the damping factor was not capable of estimating the water content as the day of the experiment changed. However, it can used to distinguish the soil types by different layer interfaces because its variance is significantly large, namely 0.007125. Note that the variances of the extracted natural frequencies, the real part of the dielectric constant, and the water content, were greater than 0.001 for all cases. Thus, we can estimate the real part of dielectric constant, the water content, by using the extracted natural frequencies. In the table, the chosen variances of the extracted poles and measured parameters

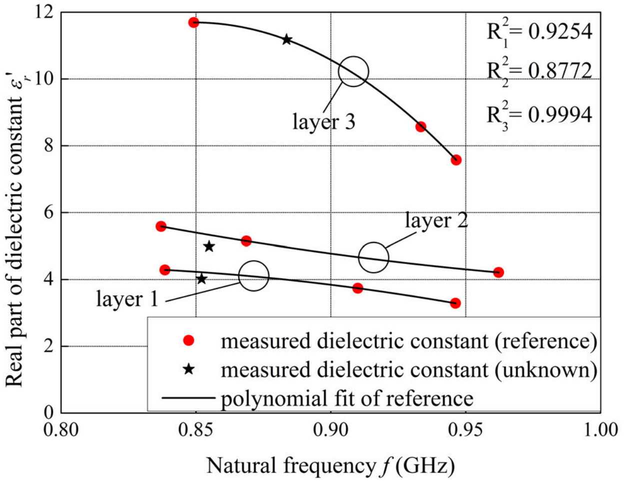

FIGURE 11. **Comparison between the real part of the dielectric constant measured by using the commercial dielectric probe kit and natural frequency extracted by using STMPM.**

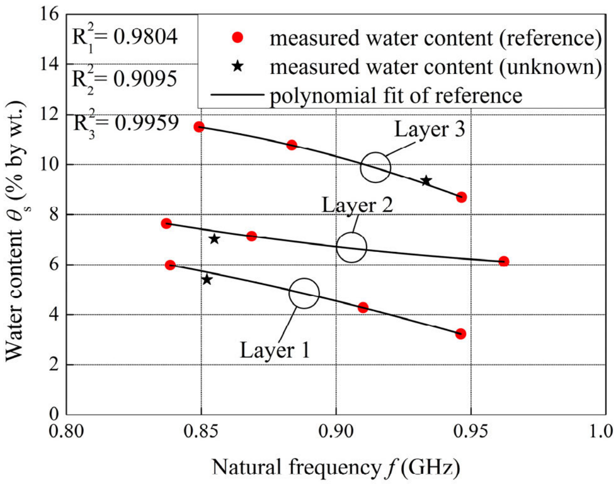

FIGURE 12. **Comparison between the soil water content measured by using the standard laboratory method and natural frequency extracted by using STMPM.**

which can be used to map the properties of the layered soil are highlighted in red.

C. MAPPING PHYSICAL AND DIELECTRIC PROPERTIES OF LAYERED SOIL

The extracted poles and measured soil properties whose variances are highlighted in red as seen in Table 2 were employed to determine their relationships. For each soil layer, the real part of the dielectric constants measured on four different days by using the commercial dielectric probe kit was plotted along with the natural frequencies extracted by using the STMPM, as shown in Fig. 11. Three of them were chosen to be the references to fit a curve with the 2nd-order polynomial. By using the least-squares method, the real part of the dielectric constants of the first, second, and third soil layers was mathematically expressed as

$$\varepsilon_{r1}' = -44.36 f_1^2 + 69.89 f_1 - 23.12 \tag{22}$$

$$\varepsilon_{r2}' = 30.24 f_1^2 - 65.37 f_1 + 39.11 \tag{23}$$

and

$$\varepsilon_{r3}' = -397.69 f_1^2 + 671.70 f_1 - 271.96, \tag{24}$$

respectively, where f_1 denotes the first order of the natural frequency in GHz, extracted by using the STMPM. Another of the four measured dielectric constants was assumed to be unknown. It was estimated after achieving the extracted natural frequency. The regression value (R^2) of 0.9254, 0.8772, and 0.9994 was achieved from the polynomial fitted plot for the first, second, and third soil layers, respectively. In the figure, R_n^2 denotes the regression value of the n^{th} soil layer. The percentage errors of the unknown dielectric constant were 5.02%, 6.96%, and 0.49% for the first, second, and third layers, respectively. These fitted equations would be very useful if one needs to estimate the dielectric constant of layered soil with a specific soil profile.

Figure 12 depicts the comparison between the soil water content measured by using the standard laboratory method and natural frequency extracted by using the STMPM. These plotted parameter values were in accordance with Table 1 as well. As seen in the previous figure, three of the measured water contents and extracted natural frequencies obtained from three experimentation days were chosen as references to fit a curve with the 2nd-order polynomial. The water contents of the first, second and third soil layers were fitted by the 2nd-order polynomial, as given by

$$\theta_{s1} = -48.43 f_1^2 + 60.84 f_1 - 10.98 \tag{25}$$

$$\theta_{s2} = 42.08 f_1^2 - 87.82 f_1 + 51.67 \tag{26}$$

and

$$\theta_{s3} = -120.73 f_1^2 + 188.05 f_1 - 61.12, \tag{27}$$

respectively. The star symbol chosen from one of the four experimental results denotes the unknown extracted natural frequency and measured water content. The R^2 of the fitted 2nd-order polynomial plots for the first, second, and third soil layers was 0.9804, 0.9095 and 0.9959, respectively. The percentage error of the unknown water content of the first, second, and third layers was 5.49%, 4.67%, and 1.51%, respectively. These fitted curves also reveal that we can rapidly map the real part of the dielectric constant and water content of the layered soil by using the extracted natural frequency obtained from the proposed GPR system, which can operate in real time.

As mentioned, the bulk density, which is a physical property of soil, obtained from the measurement on four different days was almost identical. However, the bulk density changes according to the depth profile of the soil. This implies that the soil water content strongly related to the dielectric constant does not impact bulk density. According to Table 2, it can be seen that the variances of the bulk density, the damping factor,

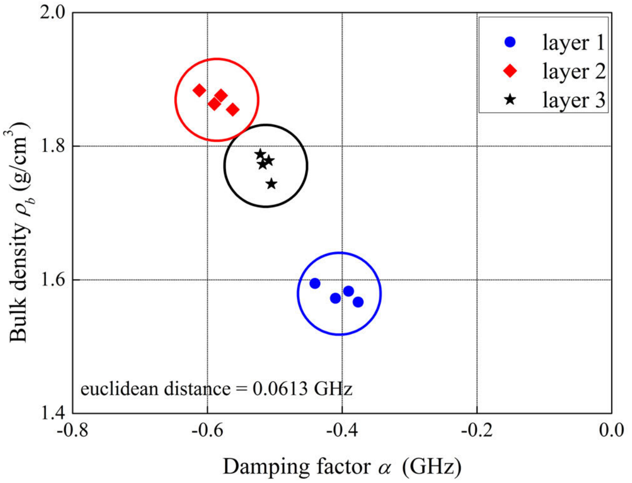

FIGURE 13. **Comparison between the soil bulk density measured by using the standard laboratory and the damping factor extracted by using STMPM.**

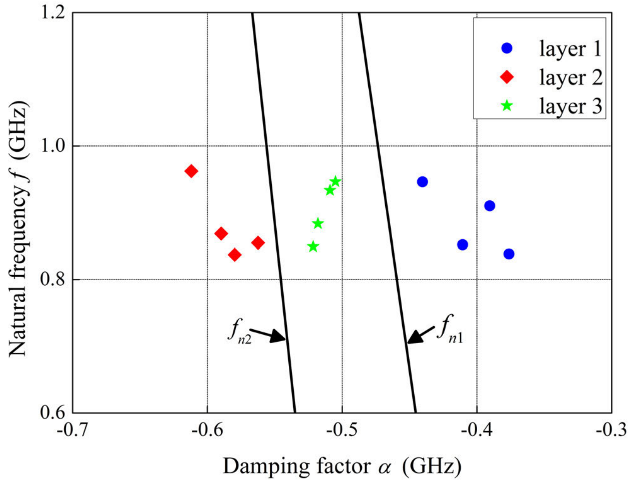

FIGURE 14. **Pole plot of three soil layers.**

and the natural frequency among three soil layers were greater than the threshold. However, the variance in the damping factor among the three soil layers was 0.007125 greater than that of the natural frequency. We therefore determined bulk density along with the damping factor instead of the natural frequency. Figure 13 shows a comparison between the soil bulk density measured by using the standard laboratory and the damping factor extracted using the STMPM. Note that the plotted values of the bulk density and damping factor of each soil layer close to each other. We cannot use curve fitting in order to map the bulk density related to the soil type with a damping factor because the soil types are not related to each other. Thus, distinguishing soil type was determined through the Euclidean distance of the point values of the bulk density and the damping factor of each soil layer. The Euclidean distance was calculated from the smallest distance between each averaged point value [23]. The circle line stands for the region of distinguishing soil type differentiated by the soil layer, which was calculated by half of the Euclidean distance.

A plot of poles, including the damping factor and the natural frequency of the three soil layers, is also shown in Fig. 14. Here, the classification using the Euclidean distance cannot be utilized because the distribution of poles is not a circle. These poles were classified using the linear support vector machine (SVM) to be three groups of soil type. The solid lines that denote the separating hyperplanes being employed as decision boundaries were expressed as $f_{n1} = -14.2308\alpha_{n1} - 5.7384$ and $f_{n2} = -18.8611\alpha_{n2} - 9.4898$ GHz. The margin perpendiculars to these hyperplanes were $2/||w_1|| = 0.2925 \times 10^8$ and $2/||w_2|| = 0.1391 \times 10^8$ [22]. One can map the poles to soil type strongly related to the bulk density by using these decision boundaries.

V. CONCLUSION

In this paper, mapping the physical and dielectric properties of layered soil by using the GPR system has been proposed. The STMPM, along with filtering and antenna calibration, were applied to extract poles from the received GPR signals. Additionally, the conjugate gradient method was introduced to solve the inverse problem in the antenna calibration process. Experiments on four different days were conducted in order to collect soil samples and GPR signals. The measured water content and dielectric constant of the soil samples collected from the four different experimentation days were significantly different, similar to the extracted natural frequency. Extracted natural frequency was therefore employed to map to the soil dielectric properties, i.e. water content and dielectric constant through 2^{nd}-order polynomial curve fitting. One of the four experimental results was assumed to be unknown and tested with the fitted curve in order to achieve the largest regression value (R^2) of 0.9959 and 0.9994 for the water content and the real part of the dielectric constant, respectively. The soil's physical property, namely the bulk density, was mapped to the extracted poles, including damping factors and natural frequencies. The linear SVM was applied to generate two straight lines in order to classify the poles of different soil types, here distinguished by soil layer interface. Additionally, it can be referred that the proposed GPR system can map the physical and dielectric properties of layered soil by using extracted poles and is suitable for precision agriculture in wide areas.

REFERENCES

[1] R. L. Raper, L. E. Asmussen, and J. B. Powell, "Sensing hard pan depth with ground-penetrating radar," *Trans. ASAE.*, vol. 33, pp. 41–46, Dec. 1990.

[2] W. Raza, S. Yousaf, A. Niaz, M. Rasheed, and I. Hussain, "Subsoil compaction effects on soil properties, nutrient uptake and yield of maize fodder (Zea mays L.)," *Pakistan J. Botany*, vol. 37, no. 4, pp. 933–940, Dec. 2005.

[3] J. A. Huisman, S. S. Hubbard, J. D. Redman, and A. P. Annan, "Measuring soil water content with ground penetrating radar: A review," *Vadose Zone J.*, vol. 2, no. 4, pp. 476–491, Nov. 2003.

[4] Y. H. Kerr, P. Waldteufel, J.-P. Wigneron, J. Martinuzzi, J. Font, and M. Berger, "Soil moisture retrieval from space: The Soil Moisture and Ocean Salinity (SMOS) mission," *IEEE Trans. Geosci. Remote Sens.*, vol. 39, no. 8, pp. 1729–1735, Aug. 2001.

[5] Y. H. Kerr, P. Waldteufel, J.-P. Wigneron, S. Delwart, F. Cabot, J. Boutin, M.-J. Escorihuela, J. Font, N. Reul, C. Gruhier, S. E. Juglea, M. R. Drinkwater, A. Hahne, M. Martín-Neira, and S. Mecklenburg, "The SMOS mission: New tool for monitoring key elements ofthe global water cycle," *Proc. IEEE*, vol. 98, no. 5, pp. 666–687, May 2010.

[6] S. Mecklenburg, M. Drusch, Y. H. Kerr, J. Font, M. Martin-Neira, S. Delwart, G. Buenadicha, N. Reul, E. Daganzo-Eusebio, R. Oliva, and R. Crapolicchio, "ESA's soil moisture and ocean salinity mission: Mission performance and operations," *IEEE Trans. Geosci. Remote Sens.*, vol. 50, no. 5, pp. 1354–1366, May 2012.

[7] D. Entekhabi, E. G. Njoku, P. E. O'Neill, K. H. Kellogg, W. T. Crow, W. N. Edelstein, J. K. Entin, S. D. Goodman, J. T. Jackson, J. Johnson, and J. Kimball, "The soil moisture active passive (SMAP) mission," *Proc. IEEE*, vol. 98, no. 5, pp. 704–716, May 2010.

[8] N. N. Das, D. Entekhabi, and E. G. Njoku, "An algorithm for merging SMAP radiometer and radar data for high-resolution soil-moisture retrieval," *IEEE Trans. Geosci. Remote Sens.*, vol. 49, no. 5, pp. 1504–1512, May 2011.

[9] M. Yang, H. Fang, F. Wang, H. Jia, J. Lei, and D. Zhang, "The three dimension first-order symplectic partitioned Runge-Kutta scheme simulation for GPR wave propagation in pavement structure," *IEEE Access*, vol. 7, pp. 151705–151712, 2019.

[10] G. Terrasse, J.-M. Nicolas, E. Trouve, and E. Drouet, "Application of the curvelet transform for clutter and noise removal in GPR data," *IEEE J. Sel. Topics Appl. Earth Observ. Remote Sens.*, vol. 10, no. 10, pp. 4280–4294, Oct. 2017.

[11] R. M. Beauchamp, D. D. Arumugam, M. S. Burgin, J. D. Bush, A. Khazendar, Y. Gim, S. Almorqi, M. Almalki, Y. A. Almutairi, A. A. Alsama, and A. G. Alanezi, "Can airborne ground penetrating radars explore groundwater in hyper-arid regions?" *IEEE Access*, vol. 6, pp. 27736–27759, 2018.

[12] J. Zheng, X. Teng, J. Liu, and X. Qiao, "Convolutional neural networks for water content classification and prediction with ground penetrating radar," *IEEE Access*, vol. 7, pp. 185385–185392, 2019.

[13] S. Garambois, P. Sénéchal, and H. Perroud, "On the use of combined geophysical methods to assess water content and water conductivity of near-surface formations," *J. Hydrol.*, vol. 259, nos. 1–4, pp. 32–48, Mar. 2002.

[14] L. Bannawat, A. Boonpoonga, and P. Akkaraekthalin, "Permittivity estimation of a shallow-layered medium using high-resolution ground-penetrating radar," *Int J Remote Sens.*, vol. 41, no. 12, pp. 4624–4641, Jun. 2020.

[15] A. Benedetto and S. Pensa, "Indirect diagnosis of pavement structural damages using surface GPR reflection techniques," *J. Appl. Geophys.*, vol. 62, no. 2, pp. 107–123, Jun. 2007.

[16] W. Shao, A. Bouzerdoum, S. L. Phung, L. Su, B. Indraratna, and C. Rujikiatkamjorn, "Automatic classification of ground-penetrating-radar signals for railway-ballast assessment," *IEEE Trans. Geosci. Remote Sens.*, vol. 49, no. 10, pp. 3961–3972, Oct. 2011.

[17] A. Benedetto and F. Benedetto, "Remote sensing of soil moisture content by GPR signal processing in the frequency domain," *IEEE Sensors J.*, vol. 11, no. 10, pp. 2432–2441, Oct. 2011.

[18] L. Bianchini Ciampoli, A. Calvi, and F. D'Amico, "Railway ballast monitoring by GPR: A test-site investigation," *Remote Sens.*, vol. 11, no. 20, pp. 1–14, Oct. 2019.

[19] R. Roberts, J. Rudy, I. Al-Qadi, E. Tutumluer, and J. Boyle, "Railroad ballast fouling detection using ground penetrating radar—A new approach based on scattering from voids," in *Proc. 9th Eur. Conf. NDT*, Berlin, Germany, Sep. 2006, pp. 1–8.

[20] L. B. Ciampoli, F. Tosti, M. G. Brancadoro, F. D'Amico, A. M. Alani, and A. Benedetto, "A spectral analysis of ground-penetrating radar data for the assessment of the railway ballast geometric properties," *NDT E Int.*, vol. 90, pp. 39–47, Sep. 2017.

[21] B. Indraratna, "1st ralph proctor lecture of ISSMGE. Railroad performance with special reference to ballast and substructure characteristics," *Transp. Geotech.*, vol. 7, pp. 74–114, May 2016.

[22] N. Chantasen, A. Boonpoonga, S. Burintramart, K. Athikulwongse, and P. Akkaraekthalin, "Automatic detection and classification of buried objects using ground-penetrating radar for counter-improvised explosive devices," *Radio Sci.*, vol. 53, no. 2, pp. 210–227, Feb. 2018.

[23] L. Bannawat, A. Boonpoonga, S. Burintramart, and P. Akkaraekthalin, "On the resolution improvement of radar target identification with filtering antenna effects," *Int. J. Antennas Propag.*, vol. 2018, pp. 1–11, Feb. 2018.

[24] A. Boonpoonga, P. Chomdee, S. Burintramart, and P. Akkaraekthalin, "Simple estimation of late-time response for radar target identification," *Radio Sci.*, vol. 52, no. 6, pp. 456–743, Jul. 2017.

[25] J. Rahman and T. K. Sarkar, "Deconvolution and total least squares in finding the impulse response of an electromagnetic system from measured data," *IEEE Trans. Antennas Propag.*, vol. 43, no. 4, pp. 416–421, Apr. 1995.

[26] A. Boonpoonga, S. Buritramart, P. Sirisuk, M. Krairiksh, and T. K. Sarkar, "Adaptive array processing unit based on direct data domain least square approach using conjugate gradient method," in *Proc. Asia–Pacific Microw. Conf.*, Bangkok, Thailand, Dec. 2007, pp. 1–4.

[27] R. Rezaiesarlak and M. Manteghi, "Short-time matrix pencil method for chipless RFID detection applications," *IEEE Trans. Antennas Propag.*, vol. 61, no. 5, pp. 2801–2806, May 2013.

[28] K. Kaemarungsi, K. Athikulwongse, K. Rungprateepthaworn, T. Duangtanoo, and P. Dangsakul, "On study of an impulse RADAR sensor for subsurface object detection," in *Proc. 12th Int. Conf. Electr. Eng./Electron., Comput., Telecommun. Inf. Technol. (ECTI-CON)*, Hua Hin, Thailand, Jun. 2015, pp. 1–6.

[29] G. C. Topp, J. L. Davis, and A. P. Annan, "Electromagnetic determination of soil water content: Measurements in coaxial transmission lines," *Water Resour. Res.*, vol. 16, no. 3, pp. 574–582, Jun. 1980.

NATTAWAT CHANTASEN (Member, IEEE) received the B.Eng. degree in computer engineering from the Mahanakorn University of Technology, Bangkok, Thailand, in 2011, and the M.Eng. degree in telecommunications engineering from the King Mongkut's University of Technology North Bangkok (KMUTNB), Bangkok, in 2013, where he is currently pursuing the Ph.D. degree. His Ph.D. degree was supported by the National Science and Technology Development Agency through the Thailand Graduate Institute of Science and Technology (TGIST). His research interests include embedded systems, ground-penetrating radar, signal processing, and radar systems.

AKKARAT BOONPOONGA (Member, IEEE) received the B.Eng. degree in electrical engineering from the King Mongkut's University of Technology North Bangkok (KMUTNB), Bangkok, Thailand, in 2002, and the M.Eng. degree in telecommunications engineering and the D.Eng. degree in electrical engineering from the King Mongkut's Institute of Technology Ladkrabang (KMITL), Bangkok, in 2004 and 2008, respectively. He is currently an Associate Professor with the Department of Electrical and Computer Engineering, Faculty of Engineering, KMUTNB. His research interests include ground-penetrating radar (GPR), radar systems, radar target identification, FPGA design, and signal processing for EM applications. He is a member of the ECTI Association. He was a Board Committee Member of the ECTI Association, Thailand, from 2016 to 2017, where he is currently a Board Committee Member.

KRIT ATHIKULWONGSE (Member, IEEE) received the B.Eng. and M.Eng. degrees from the Department of Electrical Engineering, Chulalongkorn University, Bangkok, Thailand, in 1995 and 1997, respectively, and the M.S. and Ph.D. degrees from the School of Electrical and Computer Engineering, Georgia Institute of Technology, Atlanta, GA, USA, in 2005 and 2012, respectively.

He was an Engineer with the Electricity Generating Authority of Thailand, from 1998 to 2001. Since 2012, he has been a Researcher with the National Electronics and Computer Technology Center, Pathum Thani, Thailand. His current research interests include indoor localization, ground-penetrating radar, embedded systems, physical design, computer architecture, 3-D ICs, and VLSI design.

KAMOL KAEMARUNGSI (Senior Member, IEEE) received the bachelor's degree in electronics engineering from the King Mongkut's Institute of Technology Ladkrabang (KMITL), Thailand, in 1994, the M.Sc. degree in interdisciplinary telecommunications program (ITP) from the University of Colorado at Boulder, in 1999, and the Ph.D. degree in information science from the University of Pittsburgh, in 2005. He was serving as the Thailand Chapter Chair of the IEEE Communications Society, Asia/Pacific Region 10, from 2012 to 2016. Formerly, he was the Head of the Location and Automatic Identification (LAI) Laboratory under the National Electronics and Computer Technology Center (NECTEC). He is currently the Research Director of the Communications and Network Research Group (CNWRG) under NECTEC, Thailand. His research interests include ground penetrating radar, ultrawideband sensors, wireless sensor networks, and indoor positioning systems.

PRAYOOT AKKARAEKTHALIN (Member, IEEE) received the B.Eng. and M.Eng. degrees in electrical engineering from the King Mongkut's University of Technology North Bangkok (KMUTNB), Bangkok, Thailand, in 1986 and 1990, respectively, and the Ph.D. degree from the University of Delaware, Newark, DE, USA, in 1998. From 1986 to 1988, he was a Research and Development Engineer with Microtek Products Company Ltd., Thailand. In 1988, he joined the Department of Electrical Engineering, KMUTNB. He was the Head of the Senior Research Scholar Project, which was supported by the Thailand Research Fund, from 2015 to 2017. He has authored or coauthored more than 40 international articles, more than 200 conference papers, and four books/book chapters. His current research interests include RF/microwave circuits, wideband and multiband antennas, telecommunications, and sensor systems. He is a member of IEICE, Japan, ECTI, and the EEAAT Association, Thailand. He was the Chairman of the IEEE MTT/AP/ED Thailand Joint Chapter, from 2007 to 2010, and the Vice President and the President of the ECTI Association, Thailand, from 2012 to 2013, and from 2014 to 2015, respectively. He was the Editor-in-Chief of the ECTI Transactions, from 2011 to 2013.

• • •